Obrabotka metallov (tekhnologiya, oborudovanie, instrumenty) = Metal Working and Material Science. 2026 vol. 28 no. 3 pp. 70–82
ISSN: 1994-6309 (print) / 2541-819X (online)
DOI: 10.17212/1994-6309-2026-28.3-70-82

NSTU NETI

Obrabotka metallov -
Metal Working and Material Science

Journal homepage: http://journals.nstu.ru/obrabotka_metallov

Effect of heat input during electron beam cladding on the formation of an aluminum bronze coating on stainless steel

Alexander Eliseev [a, *], *Aleksander Panfilov* [b], *Andrey Vorontsov* [c], *Anna Zykova* [d], *Andrey Cheremnov* [e]

Panin Institute of Strength Physics and Materials Science of Siberian Branch of Russian Academy of Sciences, 2/4 Akademichesky ave., Tomsk, 634055, Russian Federation

[a] https://orcid.org/0000-0001-5273-9729, alan@ispms.ru; [b] https://orcid.org/0000-0001-8648-0743, alexpl@ispms.ru;
[c] https://orcid.org/0000-0002-4334-7616, vav@ispms.ru; [d] https://orcid.org/0000-0001-8779-3784, zykovaap@mail.ru;
[e] https://orcid.org/0000-0003-2225-8232, amc@ispms.ru

ARTICLE INFO

Article history:
Received: 23 June 2026
Revised: 03 July 2026
Accepted: 16 July 2026
Available online: 15 September 2026

Keywords:
Aluminum bronze
Stainless steel
Electron beam cladding
Microstructure

Funding
This work was performed according to the Government research assignment for ISPMS SB RAS, project FWRW-2024–0001.

ABSTRACT

Introduction. The relevance of this research is driven by the need to develop technologies for applying wear- and corrosion-resistant aluminum bronze coatings onto steel surfaces to reduce the weight and cost of components while maintaining their performance in aggressive environments such as seawater. Conventional deposition methods (e.g., brazing or electroplating) fail to provide sufficient adhesion and are unsuitable for tribological components, whereas high-energy techniques require precise control of heat input and alloy composition to prevent defect formation and the development of brittle intermetallic phases. ***The purpose of this study*** is to investigate the effect of heat input during electron beam cladding on the formation of a *CuAl9Mn2* alloy coating on stainless steel. **Materials and methods.** This study employed the method of electron beam cladding of single droplets onto a steel substrate under three operating modes with different electron beam current: 30, 45, and 60 mA, corresponding to heat inputs of 135, 202, and 270 J/mm. Metallographic examination, X-ray diffraction analysis, energy-dispersive X-ray spectroscopy, and Vickers microhardness measurements were performed on the cross-sections of the deposited droplets. **Results and discussion.** It was established that with increasing heat input, the dilution ratio of the bronze by the steel increases from 2% to 59%, the penetration depth increases from 0.06 mm to 2.43 mm, and the microhardness rises from 156 HV to 343 HV. At low heat inputs, epitaxial growth of α-*Cu* is observed along with the presence of β'-Cu_3Al and γ-Cu_9Al_4 phases, indicating rapid cooling. At high heat inputs, intensive melt mixing, elemental diffusion, and the formation of iron-containing inclusions occur, leading to the predominance of α-*Cu*, α-*Fe*, and γ-*Fe* phases and the suppression of the brittle γ-phase. The obtained results demonstrate that controlled dilution during electron beam cladding can be utilized for targeted alloying and strengthening of bronze coatings, ensuring high adhesion and improved mechanical properties without the formation of defects typical of other cladding methods.

For citation: Eliseev A.A., Panfilov A.O., Vorontsov A.V., Zykova A.P. Cheremnov A.M. Effect of heat input during electron beam cladding on the formation of an aluminum bronze coating on stainless steel. *Obrabotka metallov (tekhnologiya, oborudovanie, instrumenty) = Metal Working and Material Science*, 2026, vol. 28, no. 3, pp. 70–82. DOI: 10.17212/1994-6309-2026-28.3-70-82. (In Russian).

Introduction

Aluminum bronzes are high-strength, corrosion-resistant copper alloys traditionally utilized in marine and power engineering applications, where components are subjected to abrasive wear, cavitation, and corrosion. Transitioning from monolithic bronze components to steel structures with localized bronze cladded layers enables weight reduction, increased structural stiffness, and cost savings, while retaining the required tribological and corrosion-resistant properties. This approach is particularly crucial for marine

*** Corresponding author**
Eliseev Alexander A., Ph.D. (Engineering), Scientific associate
Panin Institute of Strength Physics and Materials Science
of Siberian Branch of Russian Academy of Sciences,
2/4 Akademichesky ave.,
634055, Tomsk, Russian Federation
Tel.: +7 962 781 3745, **e-mail:** alan@ispms.ru

propellers, dies, and critical components operating in seawater, as well as for various other tribological assemblies [1].

Traditional coating methods, such as brazing, electroplating, and chemical deposition, typically yield thin coatings with poor adhesion to steel, rendering them unsuitable for tribological applications. For instance, in reference [2], steels were brazed using a *Cu–Ag* alloy in a vacuum furnace. Although this method produced a uniform layer, the adhesion was poor. Copper penetration into the steel was limited to no more than 5 μm, resulting in a copper-depleted cladding layer that was not modified by iron from the substrate. In general, achieving robust bonding between copper and steel requires high-energy input. Reference [3] demonstrated that during the wetting of steel with copper, a complex layered structure containing an oxide film develops at the interface, within which cracks propagate. Various chemical and mechanical surface modification techniques applied prior to wetting have failed to resolve this issue. Consequently, high-energy surfacing methods, such as laser or arc cladding, are currently employed to fabricate such coatings.

Laser-based methods generally provide low dilution, defect-free cladding, good adhesion, and the ability for localized property modification; however, they are highly sensitive to the reflectivity of bronze and the heat input parameters, which govern the formation of Fe-rich dendritic phases, hot cracking, and porosity [1, 4, 5].

Arc processes are highly manufacturable and allow for the deposition of thick layers. For example, in reference [6], components were fabricated by depositing *Cu–9Al–4Fe–4Ni–1Mn* wire onto an *AISI 316L* stainless steel plate, yielding a strength superior to that of the base bronze. However, when fabricating hybrid components from the same materials, reference [7] revealed substrate cracking and bronze penetration into the cracks, which was deemed a detrimental effect. Notably, a heat input of ~170 J/mm did not cause extensive substrate melting. Overall, this method frequently leads to the formation of liquation cracks [8]. Nevertheless, the use of cold metal transfer (*CMT*) arc technology has enabled the avoidance of these defects when depositing aluminum bronze coatings on *27SiMn* steel [9] and cast iron [10]. The latter study noted the beneficial effect of high heat input (up to 1,134 J/mm) and dilution (up to 40%) on coating adhesion.

In aluminum bronzes with an aluminum content of 9% or higher, slow cooling promotes the formation of the brittle **γ**-Cu_9Al_4 phase, which degrades the mechanical properties of the alloy [11]. To prevent the formation of this phase, iron and manganese are added to the alloy to stabilize the **β**-Cu_3Al phase. Consequently, iron-containing aluminum bronzes, such as *Cu–Al–Ni–Fe–Mn* system alloys, are frequently used for coating deposition in most studies. In reference [12], laser cladding of aluminum bronze powders with iron and nickel additions was performed on *AISI 316* steel. The authors did not completely eliminate the **γ**-phase, although they successfully stabilized a portion of the **β**-phase via iron addition. Due to the lack of substrate melting, iron-containing particles originating from the powder composition were present in the coating. While these particles increased hardness, it was found that coating hardness does not always correlate with wear resistance. Specifically, the most wear-resistant coating contained only 1% iron and 1% nickel. Therefore, such coatings are highly sensitive to dilution; excessive iron content leads to the formation of an excess intermetallic κ-phase in the *Cu–Al–Fe* system. This phase improves mechanical properties but reduces wear resistance due to coating delamination [13]. Strict control of dilution significantly restricts the range of permissible processing parameters and complicates their optimization. Meanwhile, insufficient heat input can result in poor coating adhesion and an undesirable martensitic microstructure in the bronze.

It is worth noting that the additive manufacturing of bulk components differs methodologically from coating deposition. In the fabrication of bulk parts, the substrate is almost always removed, and its influence is generally considered detrimental. In contrast, when depositing coatings, the substrate remains an integral part of the final component; therefore, its influence should not be adverse. From this perspective, it may be more effective to use iron-free bronzes, so that dilution of the coating with iron from the substrate becomes a beneficial rather than detrimental factor. The benefits of dilution were partially demonstrated in reference [14]. During the laser deposition of a *Cu–Al–Fe* alloy onto *AISI H13* steel, the authors showed that the absence of a transitional mixed zone between the metals is a source of defects.

In the present study, the electron beam additive manufacturing (*EBAM*) method is employed to deposit an aluminum bronze *Cu–9Al–2Mn* coating onto *AISI 321* stainless steel. Historically, this technology has been primarily used for fabricating bulk bronze components. For instance, in reference [15], *EBAM* was used to produce composite *Cu–9Al–2Mn* / *ER 321* (*0.06C–18Cr–9Ni-Ti*) components with strength exceeding that of the base alloys. Similarly, in reference [16], nickel-aluminum bronze components with high strength and corrosion resistance were fabricated using this technique. However, there is a lack of data regarding the influence of the steel substrate on the microstructure of *Cu–9Al–2Mn* coatings. ***The purpose of this work*** is to investigate the effect of heat input during electron beam cladding on the formation of a *Cu–9Al–2Mn* coating on stainless steel. To achieve this purpose, ***the following tasks*** were formulated and accomplished:

– to fabricate coating samples in the form of single droplets of *Cu–9Al–2Mn* alloy on a *AISI 321* steel substrate using electron beam cladding with varying heat inputs;

– to perform metallographic examination of the obtained samples and determination of their geometric parameters;

– to determine the phase composition of the samples using X-ray diffraction (*XRD*);

– to investigate the samples using scanning electron microscopy (*SEM*);

– to establish the effect of heat input on the microhardness of the obtained samples.

Methods

As the feedstock material for cladding, a 1.6 mm diameter wire of aluminum bronze *Cu–9Al–2Mn* was used. A 5 mm thick sheet of *AISI 321* stainless steel served as the substrate. The samples were fabricated using an experimental electron beam additive manufacturing setup equipped with an automatic wire feeder. The bronze was cladded onto the substrate in the form of single droplets. Three processing modes with different heat inputs were selected for sample fabrication. The electron beam current was varied at 30 mA, 45 mA, and 60 mA, while other processing parameters remained constant. The accelerating voltage was 30 kV, the working vacuum during the experiment was ~10^{-5} Pa, the scanning frequency was 100 Hz, and the scanning pattern was a circle with a diameter of 5 mm. The wire feed rate was 600 mm/min, and the substrate travel speed was 400 mm/min. Accordingly, with the increase in electron beam current, the heat inputs were 135 J/mm, 202 J/mm, and 270 J/mm. The heat input was calculated as the product of the accelerating voltage ***U*** and the electron beam current ***I***, divided by the substrate travel speed ***V***, as indicated in the formula for the first mode:

$$Q_{30} = \frac{U \times I}{V} = \frac{30{,}000\ \text{V} \times 0.03\ \text{A}}{\left(400/60\right)\ \text{mm/s}} = 135\ \text{J/mm}. \quad (1)$$

This approach to heat input estimation is primarily used for comparing the modes within this study and with experimental data from other works. Therefore, it does not account for the increased substrate penetration depth and metal evaporation. The schematic of the sample fabrication is presented in Fig. 1, *a*.

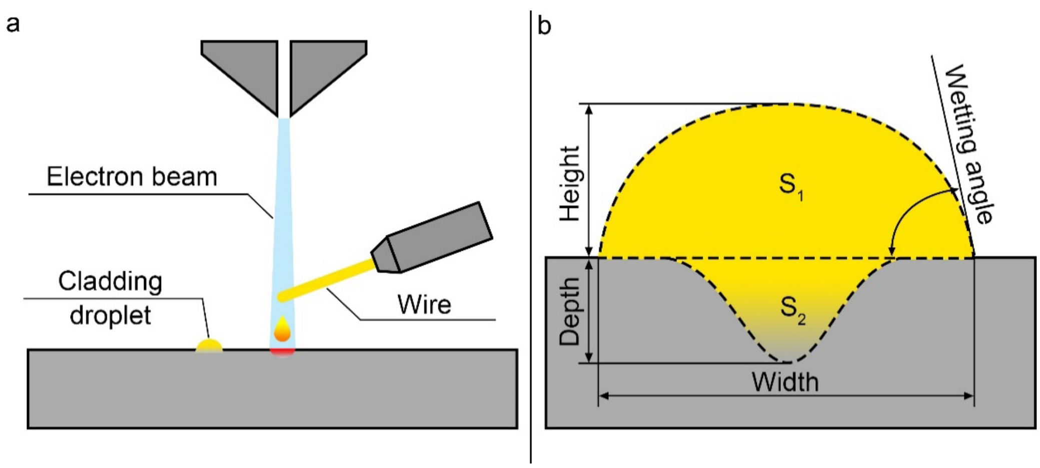

Fig. 1. Schematic of electron beam cladding (*a*) and schematic of a cladded droplet (*b*)

Microstructural examination of the obtained samples was performed using an *Olympus LEXT 4000* optical microscope (*Olympus Corporation*, Japan). The investigation was conducted on cross-sections. The samples were ground using abrasive papers up to 2,000 grit and subsequently polished on a cloth with diamond paste. To reveal the microstructure, the samples were chemically etched for 2 seconds in a solution composed of 30 ml HCl + 5 g $FeCl_3$ + 60 ml H_2O. X-ray diffraction (*XRD*) analysis was performed using a *DRON-8* X-ray diffractometer in two areas of the sample cross-sections: the upper part of the droplet and the interface with the substrate. Microhardness was measured using a *DURAMIN-5* microhardness tester (*Struers*, Denmark) according to the *Vickers* method with a load of 100 gf and a dwell time of 10 seconds. The interval between indentations was 0.2 mm. Measurements were taken across the entire height of the droplet and up to a depth of approximately 1 mm from the interface in the cross-section.

To determine the effect of the electron beam current on droplet formation, their geometric characteristics were evaluated: droplet height, width, penetration depth, and wetting angle. The schematic for measuring the geometric parameters is presented in Fig. 1,*b*. Additionally, the dilution ratio ($\boldsymbol{R_D}$) was analyzed, which determines the extent to which the volume of the deposited bronze is diluted by the steel from the substrate. This parameter is geometrically evaluated as the ratio of the melted steel area ($\boldsymbol{S_2}$) to the total area of the droplet and the molten pool ($\boldsymbol{S_1} + \boldsymbol{S_2}$) in the cross-section:

$$R_D = \frac{S_2}{S_1 + S_2} \times 100\ \%. \quad (2)$$

Results and discussion

Table presents the results of the geometric parameter measurements for the obtained samples. An increase in the electron beam current led to an increase in droplet width, penetration depth, fusion zone width, and dilution, as well as a decrease in droplet height and wetting angle. Some of these characteristics are interdependent. For instance, increasing the current from 30 mA to 45 mA increased the heat input, which likely enhanced the spreading of the droplet over the substrate, resulting in a decreased droplet height and increased width. However, further increasing the current to 60 mA did not increase the droplet width despite a continued decrease in height. This could be attributed either to spattering of the liquid metal during the deposition process or to partial evaporation of the bronze, given that the volume of the deposited bronze was constant and the substrate was monolithic. No signs of spattering were observed around the deposited bronze droplets. To confirm evaporation, the area of the droplets above the substrate surface was measured in the cross-section (denoted as $\boldsymbol{S_1}$ in Fig. 1). For the samples obtained at currents of 30 mA, 45 mA, and 60 mA, the $\boldsymbol{S_1}$ area was 6.8 ± 0.1 mm^2, 6.0 ± 0.1 mm^2, and 3.8 ± 0.1 mm^2, respectively. As shown in Table, the increase in heat input led to greater penetration but did not reduce the total volume of the molten metal filling the molten pool and forming the surface droplet. Thus, it is concluded that partial evaporation of the bronze occurred during cladding. Considering the significant difference in the melting temperatures of bronze and steel (approximately 1,050 °C and 1,400 °C, respectively), this effect is expected. The evaporation of bronze during cladding could also have contributed to a more substantial dilution of the droplet.

Geometric characteristics of the cladded samples

Current (mA)	30	45	60
Droplets height (mm)	2.14 ± 0.04	1.67 ± 0.09	1.24 ± 0.05
Droplets width (mm)	4.2 ± 0.1	5.3 ± 0.2	5.2 ± 0.1
Penetration depth (mm)	0.06 ± 0.01	0.44 ± 0.01	2.43 ± 0.09
Penetration width (mm)	1.22 ± 0.07	1.9 ± 0.1	4.4 ± 0.1
Wetting angle (°)	80.0 ± 0.6	70.6 ± 0.4	38 ± 1
Dilution (%)	2 ± 1	8.5 ± 0.5	59.6 ± 0.6

Fig. 2 shows the metallographic images of the sample cross-sections. In the lower part of the droplet (near the substrate) obtained at a beam current of 30 mA, epitaxial growth of **α**-*Cu* columnar grains is observed, whereas equiaxed grains are present in the upper part. A *Widmanstätten* structure is observed within the grains. The epitaxial growth of columnar grains is associated with the directional heat dissipation into the steel substrate during the solidification of the bronze droplet, as the cladding process is performed in a vacuum [17].

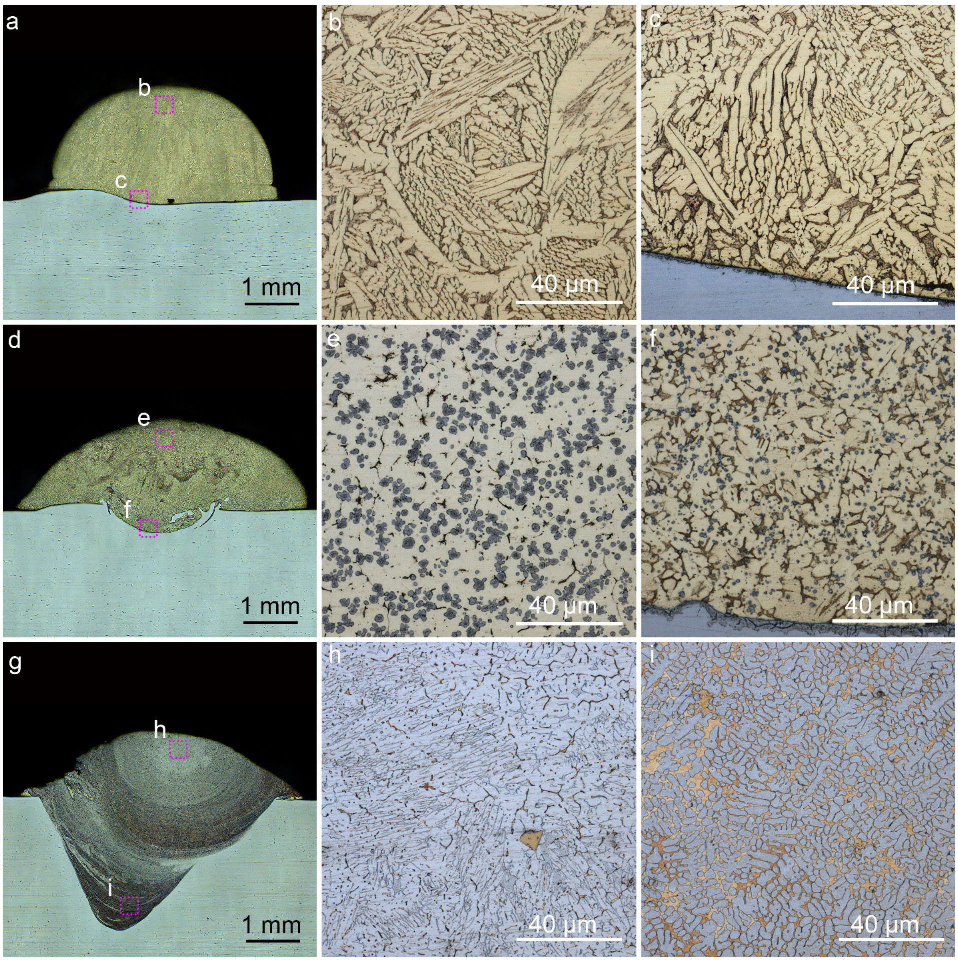

Fig. 2. Microstructure of bronze droplet samples cladded at electron beam currents of 30 mA (*a–c*), 45 mA (*d–f*), and 60 mA (*g–i*)

Microstructural analysis of the aluminum bronze droplet formed by the electron beam at 45 mA revealed the presence of iron-containing inclusions with globular and rosette-like morphologies in both the near-surface and near-bottom layers. The source of these particles is the stainless steel substrate material, which melts and migrates into the body of the deposited droplet. The combined effect of the beam on the steel substrate and the bronze brings them into a liquid state. The resulting *Marangoni* convective flows ensure mixing of the melts; however, due to the density difference between the components, stratification occurs, displacing the steel towards the upper part of the droplet [18]. Since the crystallization of the bronze alloy begins at the bottom of the weld pool, the liquid steel phase enriches the upper layers of the solidifying droplet. A similar phenomenon was observed during the selective laser melting of tin bronze *C52400* and *AISI 316L* steel in [19]. Quantitative analysis confirms the non-uniform distribution of the iron-containing particles: their volume fraction at the base of the droplet is 6 ± 1%, increasing to 20 ± 2% in the upper part. The size of the iron-containing particles in the lower part of the droplet is 1.1 ± 0.2 μm. A non-uniform distribution of steel is observed in the upper part of the droplet. Consequently, in some areas with an elevated content of substrate elements, the iron-rich particles agglomerate and form dendritic structures of various sizes. The size of the globular particles in the upper part of the droplet is 3.3 ± 0.6 μm. Since the melting and crystallization temperatures of iron are significantly higher than those of copper, the iron-containing particles crystallize earlier and hinder the coarsening of the bronze structure. In this case, the dilution of the bronze with steel led to the cessation of the epitaxial growth of columnar grains.

Increasing the electron beam current to 60 mA resulted in increased substrate penetration, a bronze dilution of 59%, and the formation of a fragmented layered structure. Throughout the droplet volume, a dendritic steel structure with bronze interlayers in the interdendritic spaces is observed. Characteristic of all samples, a modified steel layer of no more than 5 μm was observed at the molten pool interface; however, no active cracking of the steel or copper penetration along the steel grain boundaries due to liquid metal embrittlement, nor the *Kirkendall* effect, was observed [20].

Fig. 3 presents the results of the energy-dispersive X-ray spectroscopy (*EDS*) analysis of the iron-containing particles and the bronze matrix in the sample obtained at a current of 45 mA. Elemental analysis showed that during cladding, not only mechanical mixing of the steel and bronze occurred, but also mutual diffusion. Specifically, aluminum and manganese diffused into the steel, partially depleting the bronze. In turn, the bronze solid solution was enriched with 3% iron, approximately 2% nickel, and a minor amount of chromium (approximately 0.5%).

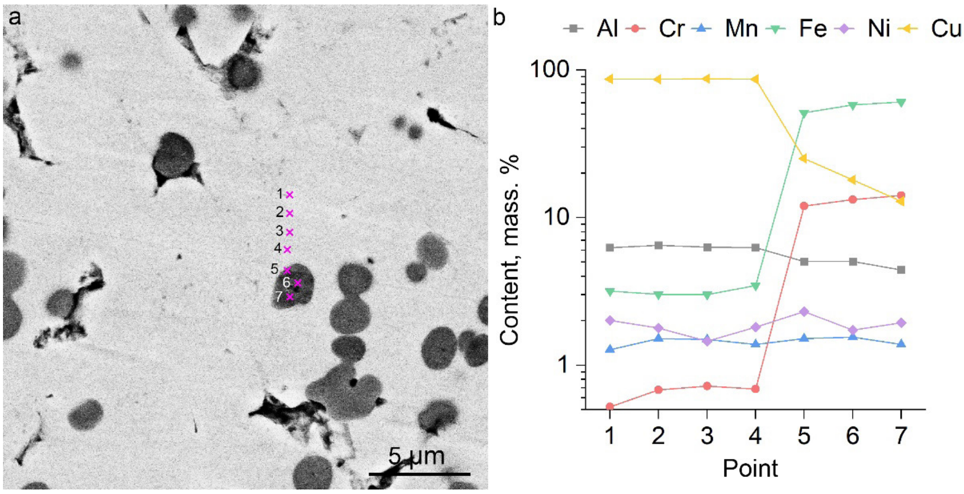

Fig. 3. SEM image of globular steel particles in the copper matrix (*a*)
and the results of energy-dispersive X-ray spectroscopy (*b*)

Fig. 4 shows the X-ray diffraction patterns of the aluminum bronze droplets. In the near-surface layer of the droplet formed at a current of 30 mA, X-ray diffraction (*XRD*) analysis identified the presence of three structural constituents: the dominant **α**-phase (*Cu*), as well as the high-temperature modifications **β′** (Cu_3Al) and **γ**(Cu_9Al_4). The retention of the metastable **β′**-phase is an indicator of a high cooling rate, which prevented the **β**-phase from completely decomposing into the eutectoid mixture (**α** + **γ**) [21]. The weak intensity of the diffraction peaks of the **γ**-Cu_9Al_4 phase indicates its minor content (approximately 4%). In the near-bottom zone, the *γ*-Cu_9Al_4 phase does not form due to more intense heat dissipation, which stimulates the growth of the **β′**-phase. The **α**-*Fe* and **γ**-*Fe* peaks registered in the diffraction patterns belong to the stainless steel substrate.

When the current was increased to 45 mA, the phase composition of the upper part of the droplet simplified to **α**-*Cu* and α-*Fe*, which fully correlates with the microstructural analysis revealing iron-containing inclusions in this region. In the lower cross-section of the droplet, exclusively the **γ**-*Fe* phase inherited from the steel substrate is registered, along with a shift in the **α**-*Cu* diffraction peaks. The disappearance of the **γ**-Fe phase in the upper layer is explained by the directional diffusion of alloying elements (Ni, Cr) from the substrate into the bronze melt. The depletion of the iron component by nickel and chromium stabilizes α-*Fe*, suppressing the formation of the **γ**-phase inherent to the substrate. Throughout the droplet volume, neither the **β′**-Cu_3Al nor the **γ**-Cu_9Al_4 phases were observed, because, as a result of diffusion into the iron,

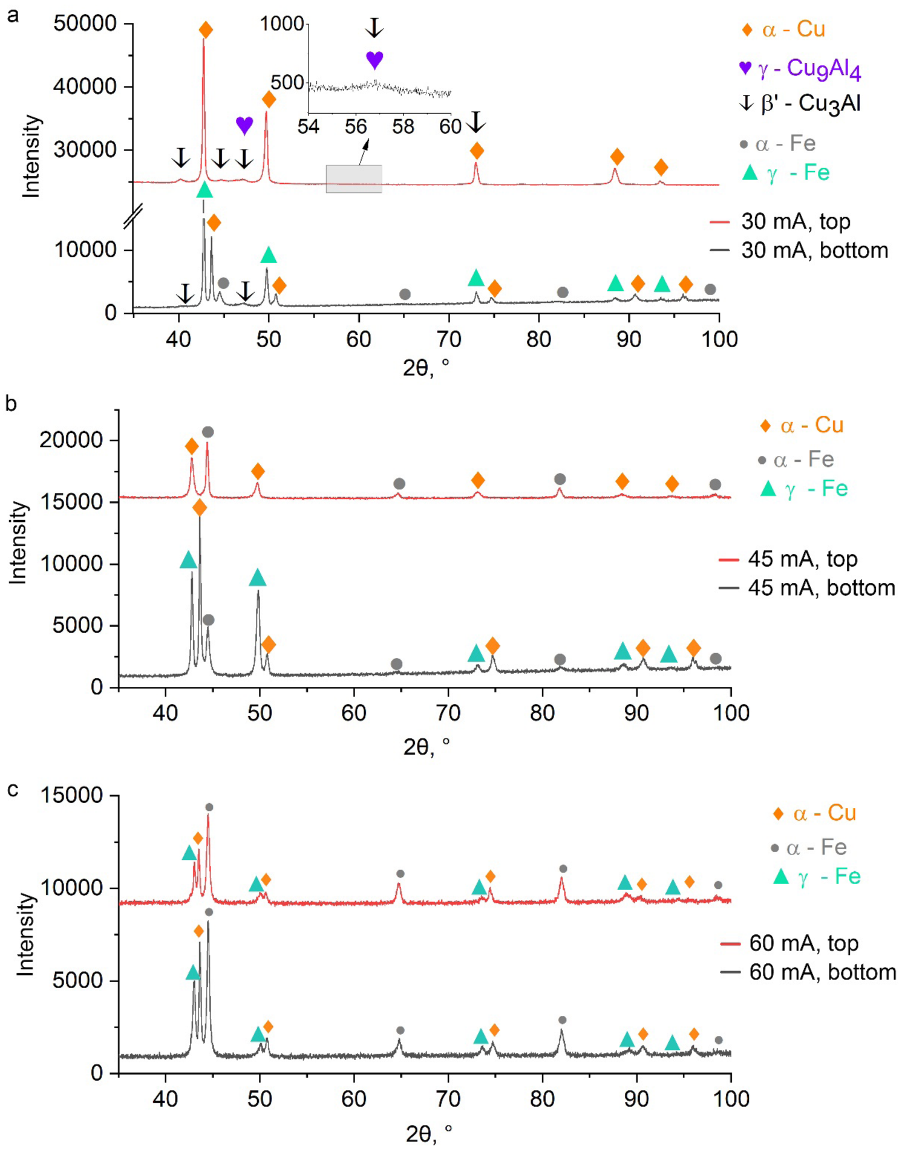

Fig. 4. X-ray diffraction patterns of samples obtained at electron beam current of 30 mA (*a*), 45 mA (*b*), and 60 mA (*c*)

the aluminum content in the bronze matrix decreased to 6%, as indicated by the point *EDS* analysis results. According to the *Cu–Al* phase diagram, only the **α**-*Cu* phase is present in this region [11]. Thus, despite the enrichment of the bronze matrix with iron, nickel, and manganese, under these conditions, the binary phase diagram can be suitable for predicting the phase state.

According to the *XRD* data, the phase composition of the aluminum bronze droplet cladded at a current of 60 mA varies insignificantly along its height. Throughout the analyzed volume of the deposited droplet, the **α**-*Cu*, **α**-*Fe*, and **γ**-*Fe* phases are registered. The retention of the high-temperature **γ**-*Fe* phase in the upper region of the droplet is a consequence of the deep melting of the steel substrate and the active involvement of its melt in convective mixing. The key factor preventing the transformation of the **γ**-*Fe* phase into the **α**-*Fe* phase is the small volume of bronze fed into the cladding zone, which is insufficient to dissolve the substrate components and stabilize **α**-*Fe*.

Fig. 5 presents the microhardness measurement results of the samples. In the sample obtained at an electron beam current of 30 mA, a stable bronze microhardness of 156 ± 6 HV is observed throughout the entire droplet height. Increasing the electron beam current to 45 mA led to an increase in microhardness to 203 ± 15 HV. However, due to the uneven mixing of the bronze and steel flows during convective processes, the microhardness was non-uniform along the droplet height. At 60 mA, the microhardness increased further to 343 ± 24 HV, with structural heterogeneity becoming more pronounced and regions

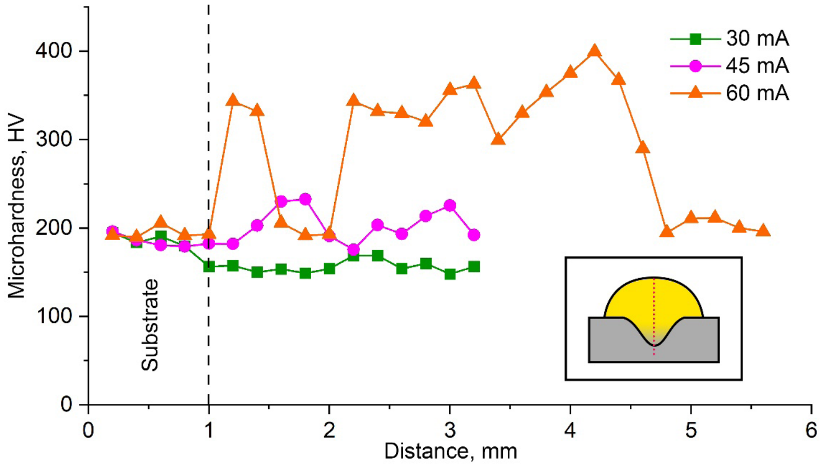

Fig. 5. Results of microhardness measurements on cross-sectional samples and a diagram of the microhardness measurement procedure

of hardness dropping to substrate levels (Fig. 2, *d*) associated with undiluted steel layers. Overall, despite such heterogeneity, higher heat inputs promote iron saturation of the bronze, thereby increasing hardness.

These results differ from the literature data. For example, in a study on electron beam printing of *Cu–8Al–6Ni* alloy components on an *X2CrNiMo17-12-2* (*0.03C–17Cr–12Ni–2Mo*) steel substrate [22], the hardness of the component decreased as the beam current increased (at similar values). The authors did not specify the possible reason for the decrease in microhardness, but they also increased the wire feed rate when increasing the beam current. Thus, the total heat input per unit of deposited metal was almost constant. Accordingly, due to the increased deposited volume, the dilution of the bronze decreased. This partially explains the discrepancy in the data. In [23], during the laser cladding of a *Cu–9.0Al–4.6Ni–3.9Fe–1.2Mn* alloy, the coating hardness increased until a heat input of 64 J/mm was reached, and then decreased. The authors of that work explain the initial increase in microhardness by the secondary particle strengthening effect. The subsequent decrease in microhardness is attributed to material overheating and microstructural coarsening, which could be caused by insufficient cooling during cladding. Furthermore, since an iron-alloyed alloy was initially used in that study, additional dilution with iron from the substrate could have led to the coagulation of the strengthening particles.

Conclusion

This study investigated the effect of heat input during electron beam cladding on the formation of a *Cu–9Al–2Mn* alloy coating on *AISI 321* stainless steel. The main conclusions can be summarized as follows:

1. It is found that increasing the electron beam current from 30 to 60 mA leads to an increase in the width and depth of penetration, as well as an increase in the dilution and spreading of the bronze droplet. It is revealed by microstructural analysis that a transition occurs from the epitaxial growth of **α**-*Cu* columnar grains at 30 mA to the formation of globular iron-containing inclusions and a dendritic iron structure at 45–60 mA, which is driven by substrate melting and convective mixing of the melts. It is also observed that, due to the density difference between the melts and convective mixing, the bronze is displaced towards the lower part of the molten pool.

2. It is confirmed by energy-dispersive analysis that mutual diffusion of elements takes place: aluminum and manganese from the bronze diffuse into the steel, while the bronze is enriched with iron, nickel, and chromium from the steel.

3. It is shown by X-ray diffraction analysis that at low currents, the high-temperature **β′**-Cu_3Al and **γ**-Cu_9Al_4 phases are retained, indicating high cooling rates, whereas at higher currents, the decrease in aluminum content to 6% leads to the dominance of the **α**-*Cu* phase and the **α**-*Fe* and **γ**-*Fe* phases.

4. It is established that the microhardness of the bronze droplets increases with the current from 156 HV to 343 HV, which is associated with strengthening due to the iron-containing particles, despite the structural heterogeneity. It is noted that the obtained data differ from some literature sources, which can be explained by the specifics of vacuum electron beam cladding and the features of the bronze–stainless steel interaction, where the strengthening mechanism due to the saturation of the matrix with iron atoms prevails, rather than softening due to structural coagulation.

References

1. Zhao L., Du B., Yao J., Chen H., Ding R., Li K. Microstructure and mechanical properties of nickel-aluminum bronze coating on 17-4ph stainless steel by laser cladding. *Chinese Journal of Mechanical Engineering*, 2022, vol. 35, p. 140. DOI: 10.1186/s10033-022-00807-z.

2. Kozlova O., Voytovych R., Devismes M.-F., Eustathopoulos N. Wetting and brazing of stainless steels by copper–silver eutectic. *Materials Science and Engineering: A*, 2008, vol. 495, pp. 96–101. DOI: 10.1016/j.msea.2007.10.101.

3. Daehn K.E., Serrenho A.C., Allwood J. Preventing wetting between liquid copper and solid steel: A simple extraction technique. *Metallurgical and Materials Transactions B*, 2019, vol. 50, pp. 1637–1651. DOI: 10.1007/s11663-019-01578-0.

4. Zhao L., Li K., Yao J., Yuan Y., Du B. The laser deposited nickel-aluminum bronze coatings on SUS630 stainless steel and its corrosion resistance in 3.5 Wt.% NaCl solution. *Metals (Basel)*, 2022, vol. 12. – P. 781. – DOI: 10.3390/met12050781.

5. Rippa F., Keller D., Freisse H., Martin N., Schudeleit T., Bambach M. Bronze-on-steel deposition with blue light high-speed laser cladding and IR laser cladding, properties and differences. *Procedia CIRP*, 2024, vol. 124, pp. 248–253. DOI: 10.1016/j.procir.2024.08.110.

6. Dharmendra C., Hadadzadeh A., Amirkhiz B.S., Janaki Ram G.D., Mohammadi M. Microstructural evolution and mechanical behavior of nickel aluminum bronze Cu-9Al-4Fe-4Ni-1Mn fabricated through wire-arc additive manufacturing. *Additive Manufacturing*, 2019, vol. 30, p. 100872. DOI: 10.1016/j.addma.2019.100872.

7. Dharmendra C., Shakerin S., Ram G.D.J., Mohammadi M. Wire-arc additive manufacturing of nickel aluminum bronze/stainless steel hybrid parts – interfacial characterization, prospects, and problems. *Materialia* (Oxf), 2020, vol. 13, p. 100834. DOI: 10.1016/j.mtla.2020.100834.

8. Dharmendra C., Shakerin S., Mohammadi M. Metallurgical assessment of additive manufactured nickel aluminum bronze-316L stainless steel bimetallic structure: Effect of deposit geometry on the interfacial characteristics and cracking. *Journal of Materials Engineering and Performance*, 2021, vol. 30, pp. 8746–8762. DOI: 10.1007/s11665-021-06194-1.

9. Qi L., Chai L., Li Z., Yang T., Zhou J., Cheng R., Zhang K. Microstructure and corrosion resistance of an Al-Bronze coating prepared by cold metal transfer on 27SiMn steel. *Surface and Coatings Technology*, 2024, vol. 478, p. 130493. DOI: 10.1016/j.surfcoat.2024.130493.

10. Meng W., Lei Y., Ma Q., Yin X., Hu L., Xie H., Guo L. Interfacial behavior and properties of aluminum–bronze coatings on ductile iron by wire-arc deposition. *Advanced Engineering Materials*, 2022, vol. 24. DOI: 10.1002/adem.202200744.

11. Hussein A.A. Structure-property relationships in dual-phase Cu-Al alloys: Part I. Individual phases. *Metallurgical Transactions A*, 1982, vol. 13, pp. 837–846. DOI: 10.1007/BF02642397.

12. Tao X.P., Zhang S., Zhang C.H., Wu C.L., Chen J., Abdullah A.O. Effect of Fe and Ni contents on microstructure and wear resistance of aluminum bronze coatings on 316 stainless steel by laser cladding. *Surface and Coatings Technology*, 2018, vol. 342, pp. 76–84. DOI: 10.1016/j.surfcoat.2018.02.032.

13. Kucita P., Wang S.C., Li W.S., Cook R.B., Starink M.J. The effects of substrate dilution on the microstructure and wear resistance of PTA Cu-Al-Fe aluminium bronze coatings. *Wear*, 2019, vol. 440–441, p. 203102. DOI: 10.1016/j.wear.2019.203102.

14. Linga H.E.S., Hatzoglou C., Zhang Y., Brøtan V., Westermann I., Ren X., Holmedal B. Directed energy deposition of aluminium bronze onto H13 steel-microstructure in multi-material additive manufacturing. *Materials Characterization*, 2025, vol. 229, p. 115603. DOI: 10.1016/j.matchar.2025.115603.

15. Semin V., Panfilov A., Utyaganova V., Vorontsov A., Zykova A. Corrosion properties of CuAl9Mn2/ER 321 composites formed by dual-wire-feed electron beam additive manufacturing. *Metal Working and Material Science*, 2024, vol. 26, pp. 163–178. DOI: 10.17212/1994-6309-2024-26.3-163-178.

16. Zhang Y., Yu H., Wang L., Wang B., Su B., Yao L., Zhao C., Cui R., Su Y. Additive manufacturing nickel-aluminum bronze alloy via wire-fed electron beam directed energy deposition: Enhanced mechanical properties and corrosion resistance compared to as-cast counterpart. *Journal of Materials Research and Technology*, 2024, vol. 32, pp. 3871–3885. DOI: 10.1016/j.jmrt.2024.08.198.

17. Chumaevskii A.V., Gurianov D.A., Osipovich K.S., Filippov A.V., Fortuna S.V., Shamarin N.N., Semenchuk V.M., Sidorov E.A., Kushnarev Yu.V., Belosludtseva A.A., Rubtsov V.E., Tarasov S.Yu., Kolubaev E.A. Application of wire and electron beam additive manufacturing for large-sized industrial products. *Physical Mesomechanics*, 2026, vol. 29, pp. 153–181. DOI: 10.1134/S102995992560123X.

18. Liu L., Wang G., Ren K., Di Y., Wang L., Rong Y., Wang H. Marangoni flow patterns of molten pools in multi-pass laser cladding with added nano-CeO_2. *Additive Manufacturing*, 2022, vol. 59, p. 103156. DOI: 10.1016/j.addma.2022.103156.

19. Bai Y., Zhang J., Zhao C., Li C., Wang H. Dual interfacial characterization and property in multi-material selective laser melting of 316L stainless steel and C52400 copper alloy. *Materials Characterization*, 2020, vol. 167, p. 110489. DOI: 10.1016/j.matchar.2020.110489.

20. Fredriksson H., Hansson K., Olsson A. On the mechanism of liquid copper penetration into iron grain boundaries. *Scandinavian Journal of Metallurgy*, 2001, vol. 30, pp. 41–50. DOI: 10.1034/j.1600-0692.2001.300106.x.

21. Culpan E.A., Rose G. Microstructural characterization of cast nickel aluminium bronze. *Journal of Materials Science*, 1978, vol. 13, pp. 1647–1657. DOI: 10.1007/BF00548728.

22. Raute J., Biegler M., Rethmeier M. Process setup and boundaries of wire electron beam additive manufacturing of high-strength aluminum bronze. *Metals (Basel)*, 2023, vol. 13, p. 1416. DOI: 10.3390/met13081416.

23. Hyatt C.V., Magee K.H., Betancourt T. The effect of heat input on the microstructure and properties of nickel aluminum bronze laser clad with a consumable of composition Cu-9.0Al-4.6Ni-3.9Fe-1.2Mn. *Metallurgical and Materials Transactions A*, 1998, vol. 29, pp. 1677–1690. DOI: 10.1007/s11661-998-0090-5.

Conflicts of Interest

The authors declare no conflict of interest.